Temporal correlation between oscillating force dipoles drives 3D single cell migration

A. Godeau, M. Leoni, J. Comelles, H. Delanoë-Ayari, A. Ott, S. Harlepp, P. Sens, Daniel Riveline

A scallop theorem for cells moving in 3D.

A. L. Godeau[1],* M. Leoni[2,3],* J. Comelles[1], H. Delanoë-Ayari[4], A. Ott[5], S. Harlepp[6], P. Sens[2],† and D. Riveline[1†]

1 *Laboratory of Cell Physics, ISIS/IGBMC, UMR 7104, Inserm, and University of Strasbourg, France*

[2] *Institut Curie, PSL, 26 Rue d'Ulm, 75005, Paris*

[3] *Université Paris-Saclay, CNRS, Laboratoire de l'accélérateur linéaire, 91898, Orsay, France*

[4] *Univ. Lyon, Université Claude Bernard Lyon 1, CNRS UMR 5306 10 rue Ada Byron, 69622 Villeurbanne Cedex, France*

[5] *Universität des Saarlandes, Biologische Experimentalphysik, Campus B2.1, D-66123 Saarbrücken, Germany and*

[6] *Tumor Biomechanics, INSERM UMR S1109, Institut d'Hématologie et d'Immunologie 1, place de l'Hôpital, 67200 Strasbourg, France*

(Dated: July 1, 2020)

The famous scallop theorem proposed by Purcell in 1977 states that self-propelled objects swimming at low Reynolds number must follow a cycle of shape changes that breaks temporal symmetry. This should hold true for crawling cells as well. However a clear mechanism for this symmetry breaking is still elusive. Here we show that cells embedded in 3D matrix form at both sides of the nucleus force dipoles driven by myosin that locally and periodically pinch the matrix. Using a combination of 3D live cell imaging, traction force microscopy and a minimal model with multipolar expansion, we show that the existence of a phase shift between the two dipoles involves mainly the microtubular network and is required for directed cell motion. We confirm this mechanism by triggering local dipolar contractions with a laser, which leads to directed motion. Our study reveals that the cell controls its motility by synchronising dipolar forces distributed at front and back. This result opens new strategies to externally control cell motion.

At cellular scales inertia is negligible. As a result low Reynolds number micro-swimmers and micro-crawlers must obey the scallop theorem, stating that the sequence of shape changes performed by self-propelled objects cannot be symmetrical in time [1–6]. Cells moving in 2D or in micro-channels often display clear spatial polarisation, characterised by F-actin flowing from the front to the back of the cell [7, 8]. The scallop theorem is obviously satisfied, and the cell velocity is directly related to the dynamics of the actin flow of the order of μm/min. Many cells, especially mesenchymal cells moving in 3D matrices, do not show such polarisation, but instead display sequences of protrusion/retraction, leading to a much slower net velocity of the order of μm/hr. The mechanism by which time-reversal symmetry is broken under these conditions remains unknown [9]. Basic principles governing 3D motion of mesenchymal cells still remain elusive.

To address this issue we designed a Cell Derived Matrix (CDM) based on [10] (Fig.1 and Material and Methods I B 1). For migration experiments, cells were embedded within a 13μm CDM layer (Fig.S1). Key molecular players are fluorescently labelled: (i) the fibronectin network within the CDM (Fig.1a); (ii) components of the cell cytoskeleton, acto-myosin and microtubules (Fig.1 a, c, d and Movies 3,5); (iii) focal contacts. Focal contacts promote adhesion and must exert local traction forces on the fibronectin network for the cell to move (Fig.S2 and Movie 4).

The CDM behaves as a soft and elastic material of elastic modulus $\approx$ 50 Pa as determined by beads embedded within the CDM and moved by optical tweezers, see Material and Methods I B 5 and Movie 1. The CDM was easily deformed by cells as they moved (Fig.1 a, b and Movies 2-3-4). This enabled us to quantify the associated matrix deformation [11] via the Kanade-Lucas-Tomasi (KLT) tracker method [12] (Fig.1 b,d). In our assay both the network deformation and the cellular machinery responsible for force-generation could be tracked simultaneously.

During observation some wild-type cells showed persistent motion while others did not move. Interestingly both motile and non-motile cells exhibited local zones of contraction-extension, equivalent to two force dipoles on either side of the nucleus (Fig.1 b). These deformations were cyclic, with periods of $\approx$ 10 mins and amplitudes of typically 2.5 μm, reminiscent of previous reports of cell autonomous contractile oscillations [13]. Periods of oscillations were comparable for motile and non-motile cells (Fig.2 g,i), see Material and Methods I B 6 for quantification of the oscillations. The phases of contraction correlated with the formation of local myosin clusters (Fig.1 c). This is consistent with the observation of distinct myosin-driven contraction centres in the migration of neurons on 2D surfaces [14]. We observed more protrusive activity at one of the two ends of elongated cells, in both motile and non-motile cells. This apparent spatial polarisation was not sufficient to elicit directed motion. We plotted the temporal cross-correlation function of contraction-extension at the two force dipoles. Strikingly, while non-migrating cells showed no clear phase shift between the two ends, with a cross-correlation peak at $t = 0$, migrating cells showed a persistent time lag

* These two authors contributed equally

† Corresponding authors: pierre.sens@curie.fr, riveline@unistra.fr

of ≈ 2 min (Fig.2 i,j). We propose that this lag is a signature of the "scallop theorem" [1], that is, a manifestation of time reversal asymmetry. As shown by Purcell, this requires at least two degrees of freedom. These are provided by the two distinct sub-cellular contraction-extension dipoles identified in migrating cells - and the forces driving them.

The most intuitive way to visualise time reversal symmetry breaking is through the existence of cycles in a properly chosen phase space, as was done in the seminal paper of Purcell [1]. This phase space may be based on a multipole expansion of the traction force exerted by the cell on its surrounding. This approach was pioneered by Tanimoto & Sano for *Dictyostelium discoideum* crawling on deformable 2D substrate [15]. In particular, they showed that cell translocation was correlated with cycles of finite area in the dipole-quadrupole phase space. In the present work, the traction forces on the matrix are analysed indirectly through a multipole expansion of the rate of matrix deformation. Briefly (see details in Material and Methods I B 7), we extracted the substrate velocity vector field $u_i^{(n)}$ for the component i of the change of substrate deformation between two consecutive frames at position n of the mesh. The dipole is a tensor defined as $S_{ij} = \frac{D_{ij}+D_{ji}}{2}$ with $D_{ij} = \sum_n \Delta_i^{(n)} u_j^{(n)}$, where $\Delta_i^{(n)}$ is the i-th component of the vector joining the cell centre and the point n on the mesh. Similarly, the quadrupole tensor is defined as $Q_{ijk} = \sum_n \Delta_i^{(n)} \Delta_j^{(n)} u_k^{(n)}$. We then consider the projection of these quantities on the main axis identified by the average direction of the cell trajectory and we call these components the main dipole, D, and the main quadrupole, Q.

We determine the time variation of the dominant components of the dipole and quadrupole matrices. The dipole/quadrupole observed for non-migrating cells are comparable in magnitude to those of migrating cells

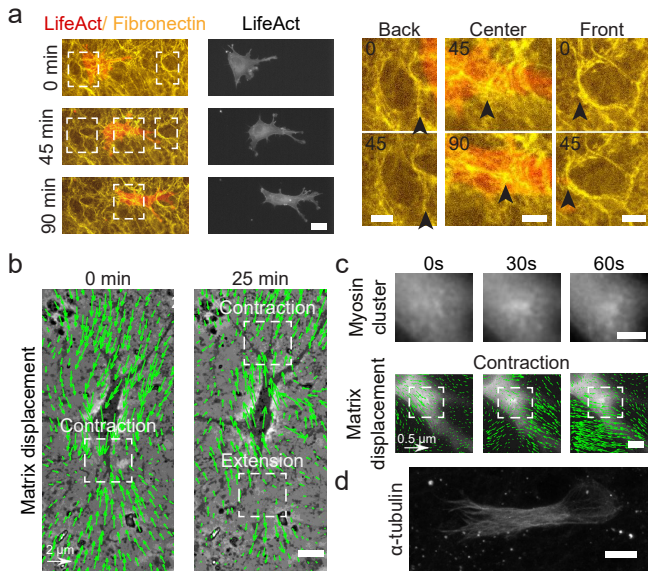

FIG. 1. Key players in cell motility. a) Left panel (and Movie 4): A cell deforms the fibronectin (FN) network when migrating (FN in yellow and mCherry LifeAct for actin filaments in red). Right panel: Enlargement of the white windows of the left panel. Black arrows highlight displacement of fibers due to cell movement. b) Overlay of phase contrast image and KLT calculation of mesh displacement (green arrows - with scale bar shown) with local contraction and extension dipoles indicated with white windows. c) Myosin clusters form locally within cells and are correlated with local contraction. Bottom: KLT deformation (green arrows) and myosin mCherry signal. Top: Enlargement of the white window of the bottom panel showing the myosin mCherry signal. d) α-tubulin staining of a cell inside CDM. Microtubules extend from the centrosome to the periphery of the cell (see also Movie 5). In panels, scale bars: (a) 25 μm (b,c,d) 10 μm.

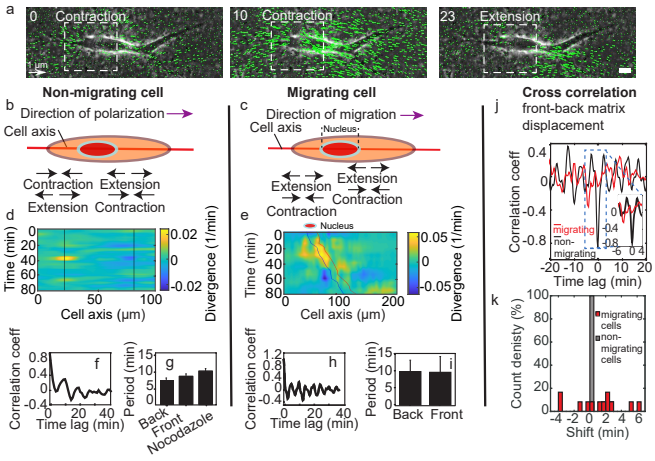

FIG. 2. Dynamics of matrix deformation for migrating and non-migrating cells. a) Snapshots overlaying phase contrast images and KLT calculation of matrix rate of deformation (green arrows) showing a contraction/extension center, scale bar 10 μm. b-c) Schematics of the alternating phases of contraction and extension for a non-migrating cell (b) and a migrating cell (c). d-e) Heatmap of the divergence of the corresponding matrix displacement. Contractile and extensile force dipoles correspond to blue and yellow spots, respectively. Non-migrating cells (c) show two oscillating dipoles (their centres are approximately indicated by the solid black lines) that appear to be in phase opposition, while migrating cells (d) show a more complex spatio-temporal pattern. The blue and red solid lines in (e) indicate the two sides of the nucleus. f) Typical correlation function of the contraction-extension time series at the back of non-migrating cells, with a first peak at ≈ 5 min. g) Average periods of contraction-extension cycles, which is similar (≈ 7−8 min) at the front and back of the cell, and slightly higher (≈ 9.5 min) for nocodazole treated cells, which show no permanent cell polarisation. h) Correlation function at the back of migrating cells, with a first peak at ≈ 10 min. i) Average period of the contraction-extension cycles for migrating cells. j) Typical cross-correlation function between back and front rates of deformations. k) Distribution of the values of the time-lag for migrating and non-migrating cells (with $n_{mot} = 12$ motile cells, $n_{nomot} = 8$ motile cells, and $N > 3$ biological repeats).

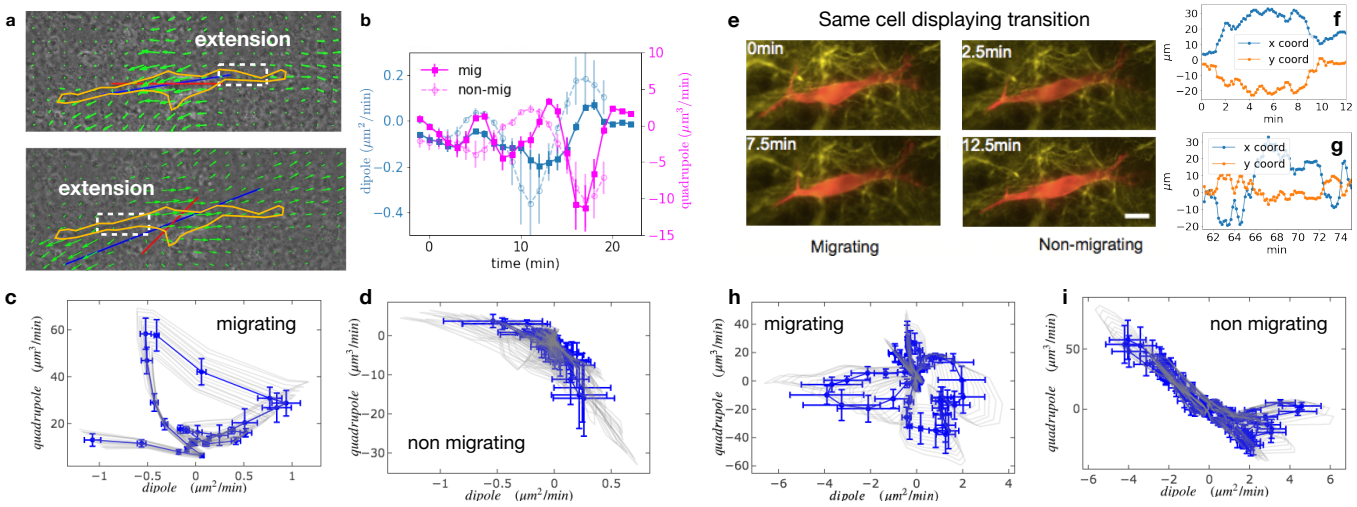

FIG. 3. Multipole analysis of the matrix deformation rate. a) Snapshots of a cell with: matrix rate of deformation, green arrows, the main dipole axis, blue, the axis of the cell motion, red. b) Time series of the main dipole, blue, and quadrupole, magenta, - projected on the cell axis - for a migrating cell (squares) and a non-migrating cell (circles), sampling approximatively 1/10 of the duration of the entire experiment. c-d) Cell trajectory in the dipole/quadrupole phase space for a migrating cell (c) and a non-migrating cell (d). The migrating cell follows a cycle with a finite area and the non-migrating cell does not. The error bars are obtained following the procedure described in Material and Methods I B 7. The individual cycles for different radii are shown in light gray. e) Snapshots of a cell which in the course of the same experiment displays a transition from migrating to non-migrating behaviour (Lifeact in red and fibronectin in yellow), scale bar 10μm. (f-g) Cell positions in the x-y plane (blue and orange curves) during the migrating phase (f - migration mainly along the x-axis) and the non-migrating phase (g - absence of net cell motion). (h-i) Cycles for this cell in the dipole/quadrupole phase space during the migrating (h) and non-migrating (i) phases, showing the same difference in area (see also Movie 7).

(Fig.3 a,b). This shows that the absence of migration is not due to the lack of traction forces (see also Fig.S4). The cell trajectory represented in the dipole/quadrupole phase space showed a cycle enclosing a finite area for migrating cells, but a vanishing area for non-migrating cells (Fig.3 c,d, and more examples Fig.S5). To further test the relationship between finite cycle area and motility of individual cells, we analyzed the migration of the *same* cell that underwent motion and then stopped (Fig.3 e-i and Movie 7). Strikingly, we observed that the cycles switched from a finite area while the cell was moving to a vanishing area when the cell stopped (Fig.3 h, i). The finite area is a direct illustration that the phase shift between the contraction-extension cycles at the two ends of migrating cells observed in Fig.2j,k also manifests itself in the traction force pattern exerted by the cell on the matrix through focal contacts. This is a clear signature of time reversal symmetry breaking.

To determine whether we could relate the correlation between the oscillations at the two cell ends with molecular actors, we tracked cell motion in the presence of the microtubule depolymerizing agent, nocodazole. Nocodazole treated cells undergo oscillations driven by local force dipoles with typical periods $\sim$ 10min (Fig.2 g) but do not maintain a fixed cell-polarization (Movie 12). In this case, oscillations at different cell ends were anti-correlated, and cells did not show directed motion. This further supports the notion that a coupling between oscillators is needed to promote directed motion. This also suggests that the microtubule network, itself, is a crucial element impacting on the correlation and time delay between oscillations across the cell, which in turn break the cell symmetry and promote cell locomotion. This result is consistent with the notion that the microtubular network regulates the polarity of migrating cells [16, 17].

The geometry and dynamics of the traction force distribution suggest a direct comparison with models of self-propelled objects made of discrete moving beads [2, 3, 5, 6]. Fig.4a,b displays an idealised cell with two pairs of beads exerting time-shifted oscillatory force dipoles at its two ends. The cell activity is characterised by the amplitude d and period T of the oscillations and a phase shift $\psi = 2\pi\Delta T/T$ between oscillations at the two ends. The simplest self-propelled object is a microswimmer embedded in a fluid matrix and migrating due to hydrodynamic interactions [2, 3, 5]. In this case, the period of oscillation is the only time scale in the problem and, in the limit of small oscillation amplitudes, the net cell velocity over a cycle follows the scaling [5]

$$V_{swim} = \frac{d^2}{L_s T} f_s(\psi) \qquad (1)$$

where $f_s(\psi)$ is a periodic function of the phase shift satisfying $f_s(\psi = 0) = 0$, *i.e.* no velocity without phase shift, as required by the scallop theorem, and $L_s \propto r^4/(aD^2)$ is a length scale entirely set by the cell geometry (r is

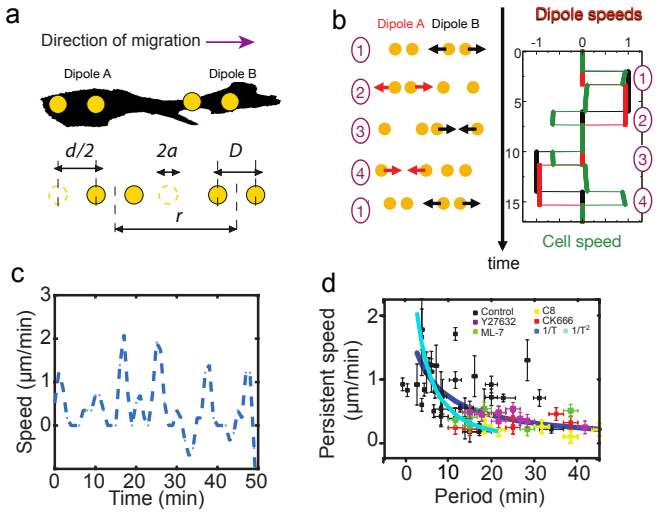

FIG. 4. Persistent speed is related to the period of oscillations. a) Schematics of dipoles distribution highlighting quantities used in the theoretical model: two dipolar units ("A" and "B") made up of disks of radius a, through which cells exert traction forces on the extracellular environment. The dipoles, at distance r apart, oscillate with period T, with minimum amplitude D and a maximum amplitude $D + d$. b) Model dynamics. Left: Alternate phases of extension/contraction are imposed to the two dipoles, defining a cycle ("1, 2, 3, 4, 1..") that is not time-reversible. Right: the extension/contraction rates of dipole "A" and "B" are shown in red and black, respectively, in unit d/T. The cell velocity, calculated using the model discussed in [5], is shown in green in the same units. It oscillates between positive and negative values - with a non-vanishing mean - with a period equal to that of individual dipoles. c) Typical plot of the experimentally measured instantaneous speed of a migrating cell over time, showing oscillation with a non-vanishing mean. d) Persistent speed as a function of speed period for control cells and cells treated with specific cytoskeleton inhibitors: 10μM ROCK inhibitor Y-27632; 10μM MLCK inhibitor ML-7; 100 μM lamellipodia growth promoter C8 [18] and 50 μM Arp2/3 inhibitor CK666, see Material and Methods I B 2. Each data point corresponds to one cell. The plot displays a decay consistent with a power law. The continuous lines show the fits for $V \sim 1/T$ (dark blue) and $V \sim 1/T^2$ (light blue), following Eqs.(1,2).

the distance between the dipoles, D the dipole size and a the bead size - Fig.4 a).

A key aspect of cell crawling, which is absent for microswimmers, is the dynamics of cell attachment and detachment from the surrounding matrix. Our results suggest that dipole contraction is associated with an active contraction of acto-myosin clusters and that dipole extension corresponds to the elastic relaxation of the CDM following local cell detachment, *i.e.* the loss of focal contacts, see Movie 4 and [19]. The kinetics of cell binding/unbinding to the extracellular matrix defines additional dynamic parameters, which can at the simplest level, be captured by a velocity scale v_{adh} [6]. For cells crawling on a rigid substrate - and in the limit of small oscillation amplitudes and fast binding kinetics - the net crawling velocity can be written as [6]:

$$V_{crawl} = \frac{d^3}{v_{adh} L_c T^2} f_c(\psi) \qquad (2)$$

where $f_c(\psi = 0) = 0$ as for swimmers, and the length-scale $L_c \propto r^2/a$ also includes additional dimensionless factors related to substrate dissipations (see [6] for more details). These simple models predict how the velocity should depend on the period of oscillation T. The result depends on whether the amplitude of oscillations d is fixed or depends on T. For oscillations of constant amplitude, the net velocity of both swimmers and crawlers decreases if the period of oscillation increases. On the contrary, the velocity is expected to increase with the period if the amplitude increases linearly with the period: $d \sim T$, as can be expected if the self-propelled object operates under constant force - or equivalently constant contraction/extension rate.

The temporal oscillations of the instantaneous cell velocity is a good readout for the dynamics of the internal force generation. For such self-propelled objects, the instantaneous velocity oscillates around the average values given by Eqs.1 or 2 with a time dependence that reflects the dynamics of the underlying force dipoles. An example of such (theoretical) velocity oscillations can be seen on Fig.4 b. Experimental observations indeed report strong oscillations of the instantaneous cell velocity (Fig.4 c).

To test how the period of oscillation of migrating cells influenced their velocity, we tracked cell motion for a variety of specific inhibitors that impact on oscillation periods, see Material and MethodsI B 6, Fig.S3 and Movies 10-12. We plotted the cell velocity as a function of oscillation period for all conditions (Fig.4 d). An inverse correlation between period and velocity is evident from the data. This is consistent with locomotion being driven by controlling cell deformation instead of cell traction forces. Similar conclusions have been reached in the different context of adherent epithelial cells [20].

Altogether, these results suggest that the temporal coupling between spatially distributed force dipoles along the cell promotes cell motion. To verify this, we needed to find a way to externally trigger localised cellular force dipoles. We leveraged the fact that localized laser ablation led to the recruitment of actin cytoskeleton and localised cell contraction associated to a pinching of the matrix (Fig.5 a-b and Movie 8). We then used this method to locally impose cellular force dipoles, by triggering local contractions alternatively at either sides of the cell. We imposed correlated contractions by selecting a constant time interval between consecutive laser ablations: this triggered translocation. This shows that externally induced force-dipoles are sufficient to promote directed cell motion (Fig.5 c-d and Movie 9).

Acto-myosin complexes are likely to be the functional elements that control the dynamics of the individual contractile units. Remarkably, the dynamics of individual dipoles appear similar in migrating and non-migrating

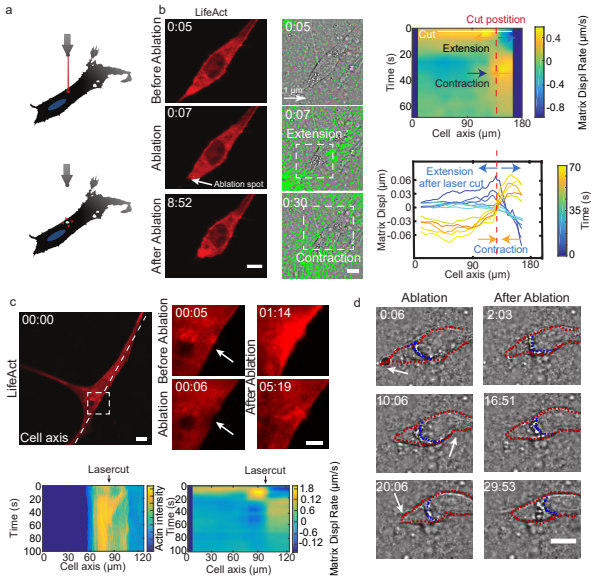

FIG. 5. Cell motion is triggered by means of laser induced force dipoles. a) Schematic of laser ablation experiment. b) (Left panel: Lifeact, middle panel: phase contrast and KLT) Ablation at the back of the cell (white arrow) immediately followed by an extension, and later by a contraction of the matrix, (both highlighted using white square window). scale bar LifeAct: 10 μm KLT: 20 μm. Right panel. Bottom: Plot of the displacement rate along the cell axis at different time (colour coded) showing extension and contraction. Top: Heatmap of displacement rates indicating the initial extension and the subsequent contraction. c) Top: sequence of snapshots during laser ablation on cell expressing mCherry LifeAct. Intensity drops locally immediately after the cut, followed by a local recruitment of actin, scale bar 20 μm, scale bar in zoom 5 μm. Bottom: the intensity heatmap reveals a focused actin flow (see also Movie 8). As shown in the deformation map, the contraction precedes this flow. d) Consecutive ablations (indicated with white arrows) mimics contraction-extension cycles at the front and back of cell. Ablation is performed in the following order: at the cell back, at the front and then at the back again. In all panels, scale bar 10μm and time in $mm:ss$. Note cell motion to the right (see also Movie 9), scale bar 10 μm. The cell is outlined in red and the back of the nucleus with a blue dashed line.

cells, suggesting that the same force generation machinery is equally active in both types of cells, and that it is the *synchronisation* between individual units that makes movement possible. Altering the dynamics of individual units can affect motion, in particular, faster oscillations can lead to faster motion, but the coordination between units is key in enabling cell translocation.

Acto-myosin networks commonly show oscillatory dynamics *in vitro* and *in vivo* in a variety of systems and over a large range of length scales [13]: single filaments in motility assays [21–23], cells [24] and cell fragments [25], and even entire organisms [26]. The biological function of these generic dynamics is often unclear. However in our case, they appear to be essential. Fast oscillations could lead to quicker motions, and we conjecture that cellular systems could adapt their velocity by modulating the oscillation period. In this context, it would be interesting to test this proposal by combining tracking of single moving cells and local matrix deformations *in vivo*. If confirmed, this would provide an outstanding example of a physiological relevance for such oscillations.

The phase-shift between contractile units encodes cell polarity. Its maintenance in the course of time requires the existence of a polarity memory. If this type of phase locking can be expected in non-linear systems [27], it is more demanding in the cellular context, where it is challenged by strong fluctuations in protein concentrations and activities. Our results suggest that the microtubular network is involved. However, other cytokeletal elements and their interplay with adhesion dynamics are likely to play a role as well. Disentangling the interplay between mechanics and biochemical regulation in this process remains an important open question.

We propose that temporal correlations between distinct contraction-extension units along the cell body is a general principle used by mesenchymal cells to achieve directional motility in 3D. This suggests new strategies to control the motion of cell by externally modulating the local contractile activity, for which we give a proof-of-principle using a standard laser setup. This concept could also be used to design synthetic micro-crawlers. Whereas there exists many examples of artificial micro-swimmers (see [28] for a review), there is to our knowledge no realisation of micro-crawler in regimes where inertia is negligible.

ACKNOWLEDGMENTS

We thank the Riveline Lab. for discussions and help, M. Maaloum, the Imaging and Microscopy Platform of IGBMC, and H.P. Erickson, A. Huttenlocher, E. Paluch for constructs, J. Goetz for the former CDM protocol and M. Piel for critical reading of the manuscript. D.R. acknowledges support from CNRS (ATIP), ciFRC Strasbourg, the University of Strasbourg, Labex IGBMC, Foundation Cino del Duca, Région Alsace, Saarland University. A. Ott and D. Riveline acknowledge support from DFH-UFA through the Collège Doctoral Franco-Allemand CDFA-01-13. This study with the reference ANR-10-LABX-0030-INRT has been supported by a French state fund through the Agence Nationale de la Recherche under the frame programme Investissements d'Avenir labelled ANR-10-IDEX-0002-02. M.L. acknowledges financial support from the ICAM Branch Contributions and Labex CelTisPhyBio N^o ANR-10-LBX-0038 part of the IDEX PSL N^o ANR-10-IDEX-0001-02 PSL. A. Ott acknowledges support by DFG within the collaborative research center SFB 1027.

[1] E. M. Purcell, American Journal of Physics **45**, 3 (1977).
[2] A. Najafi and R. Golestanian, Phys Rev E Stat Nonlin Soft Matter Phys **69**, 062901 (2004).
[3] R. Golestanian and A. Ajdari, Phys Rev E **77**, 036308 (2008).
[4] N. P. Barry and M. S. Bretscher, Proc Natl Acad Sci USA **107**, 11376 (2010).
[5] M. Leoni and P. Sens, Phys. Rev. E **91**, 022720 (2015).
[6] M. Leoni and P. Sens, Phys. Rev. Lett. **118**, 228101 (2017).
[7] L. Barnhart *et al.*, PloSBiology **9**, e1001059. (2011).
[8] Y.-J. Liu, M. Le Berre, F. Lautenschlaeger, P. Maiuri, A. Callan-Jones, M. Heuzé, T. Takaki, R. Voituriez, and M. Piel, *Cell*, Cell **160**, 659 (2015).
[9] K. M. Yamada and M. Sixt, Nature Reviews Molecular Cell Biology **20**, 738 (2019).
[10] E. Cukierman, R. Pankov, D. R. Stevens, and K. M. Yamada., Science **294**, 1708 (2001).
[11] H. Delanoe-Ayari *et al.*, Cytoskeleton **65**, 314 (2008).
[12] B. D. Lucas and T. Kanade, International Joint Conference on Artificial Intelligence , 674 (1981).
[13] K. Kruse and D. Riveline, Current Topics in Developmental Biology **95**, 67 (2011).
[14] J. Jiang, Z. Zhang, X.Yuan, and M. Poo, J. Cell Biol. **209**, 759 (2015).
[15] H. Tanimoto and M. Sano, Biophys. J. **106**, 16 (2014).
[16] S. Etienne-Manneville, Traffic **5**, 470 (2004).
[17] I. Kaverina and A. Straube, Seminars in cell & developmental biology **22**, 968 (2011).
[18] I. Nedeva, G. Koripelly, D. Caballero, L. Chieze, B. Guichard, B. Romain, E. Pencreach, J.-M. Lehn, M.-F. Carlier, and D. Riveline, Nat Commun. **4**, 2165 (2013).
[19] A. Godeau, H. Delanoë-Ayari, and D. Riveline, Methods Cell Biol. **156**, 185 (2020).
[20] A. Saez, A. Buguin, P. Silberzan, and B. Ladoux, Biophysical journal **89**, L52 (2005).
[21] D. Riveline, A. Ott, F. Julicher, D. A. Winkelmann, O. Cardoso, J. J. Lacapere, S. Magnusdottir, J. L. Viovy, L. Gorre-Talini, and J. Prost, Eur Biophys J. **27**, 403 (1998).
[22] P.-Y. Plaçais, M. Balland, T. Guérin, J.-F. Joanny, and P. Martin, Phys Rev Lett **103**, 158102 (2009).
[23] D. Gillo, B. Gilboa, R. Gurka, and A. Bernheim-Groswasser, Phys. Biol. **6**, 036003 (2009).
[24] J. Negrete *et al.*, Phys. Rev. Lett. **117**, 148102 (2016).
[25] E. Paluch, M. Piel, J. Prost, M. Bornens, and S. C., Biophys J. **89**, 724 (2005).
[26] A. C. Martin, M. Kaschube, and E. F. Wieschaus, Nature **457**, 495 (2009).
[27] A. Pikovsky, M. Rosenblum, and J. Kurths, *Synchronization: A Universal Concept in Nonlinear Science* (Cambridge University Press, 2002).
[28] J. Elgeti, R. G. Winkler, and G. Gompper, Reports on Progress in Physics **78**, 056601 (2015).

I. SUPPLEMENTARY MATERIALS

A. Supplementary figures

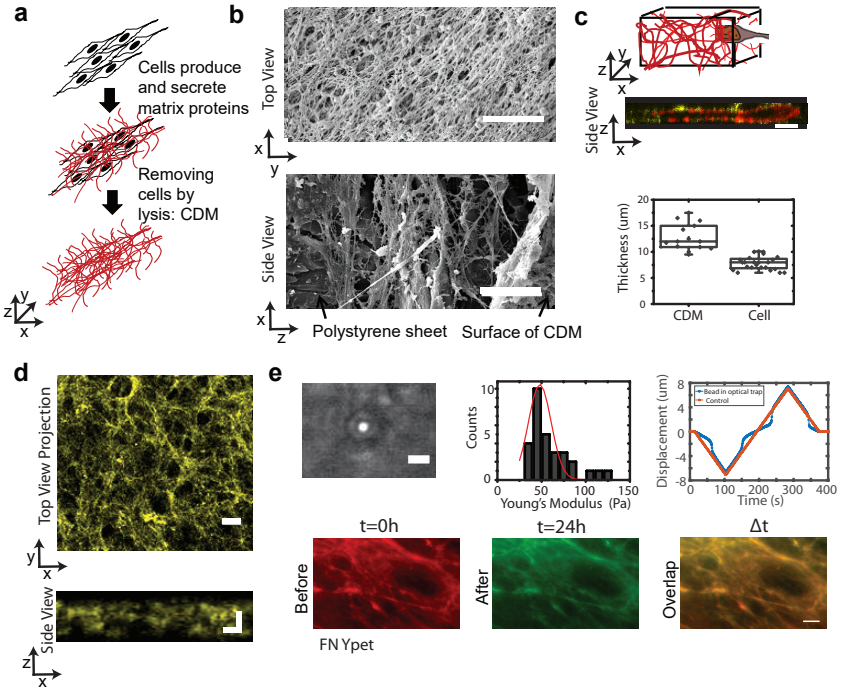

FIG. S1. Characterization of CDM. a) Schematics of the CDM preparation: Cells are cultured on a gelatin based surface during eight days and then removed by lysis. b) Electron microscope images of the top layer ($x-y$) and the side view ($x-z$) of CDM; despite the high density of the top layer, cells enter within minutes; scale bars 10μm. c) Cells are embedded in the CDM. Top: schematic; middle: a typical image with actin in red and fibronectin in yellow; bottom : cell thickness is $7.8 \pm 0.3\mu$m compared to CDM thickness $12.8 \pm 0.7\mu$m d) Typical image of fibronectin labeling within CDM. Top, view in the $x-y$ plane (scale bar: 20μm) and, bottom, side view in the $x-z$ plane (scale bar: 10μm). e) Top row : Rheological characterization of the CDM by optical tweezer (see Movie 1). To perform the measurements at the location where cells apply forces, a 1μm size bead is placed in the CDM and trapped in the laser beam of an optical tweezer, scale bar: 5μm. The stage is moved back and forth (see also Movie 1). Distribution of the Young Modulus shows a mean value of 50 Pa Trapping and untrapping curves of the bead (blue curve) show that bead movement is symmetric, suggesting that the CDM is essentially an elastic material. Bottom row : the CDM keeps its shape over time; CDM was visualized before at $t = 0$ (red) and after the cell passage at $t = 24h$ (green); the merged image (last panel) shows that the CDM network remains unchanged. Scale bar: 10μm.

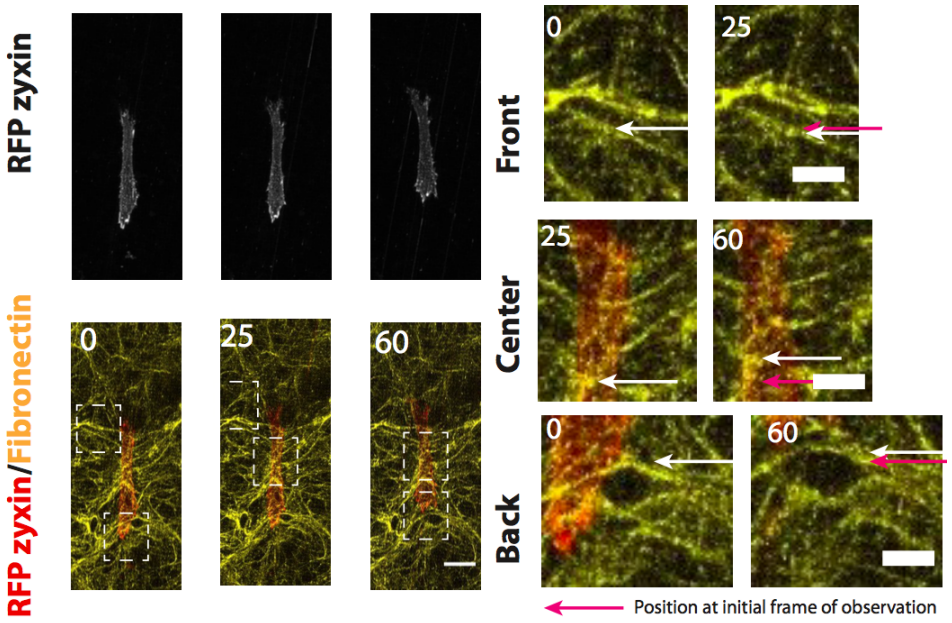

FIG. S2. Cells deform the CDM network by passing through the network and by exerting local forces through focal contacts. FN in yellow and cell expressing RFP-zyxin, scale bar 25μm. Right side shows a blow up of one the zones highlighted by the squares, scale bar 5μm. White arrows show the movement of a FN fiber, taken at two consecutive instants of time. Bottom panels : The enlargement of a pore behind the cell suggests a local pulling force by the cell, mediated by focal contacts. Time in min.

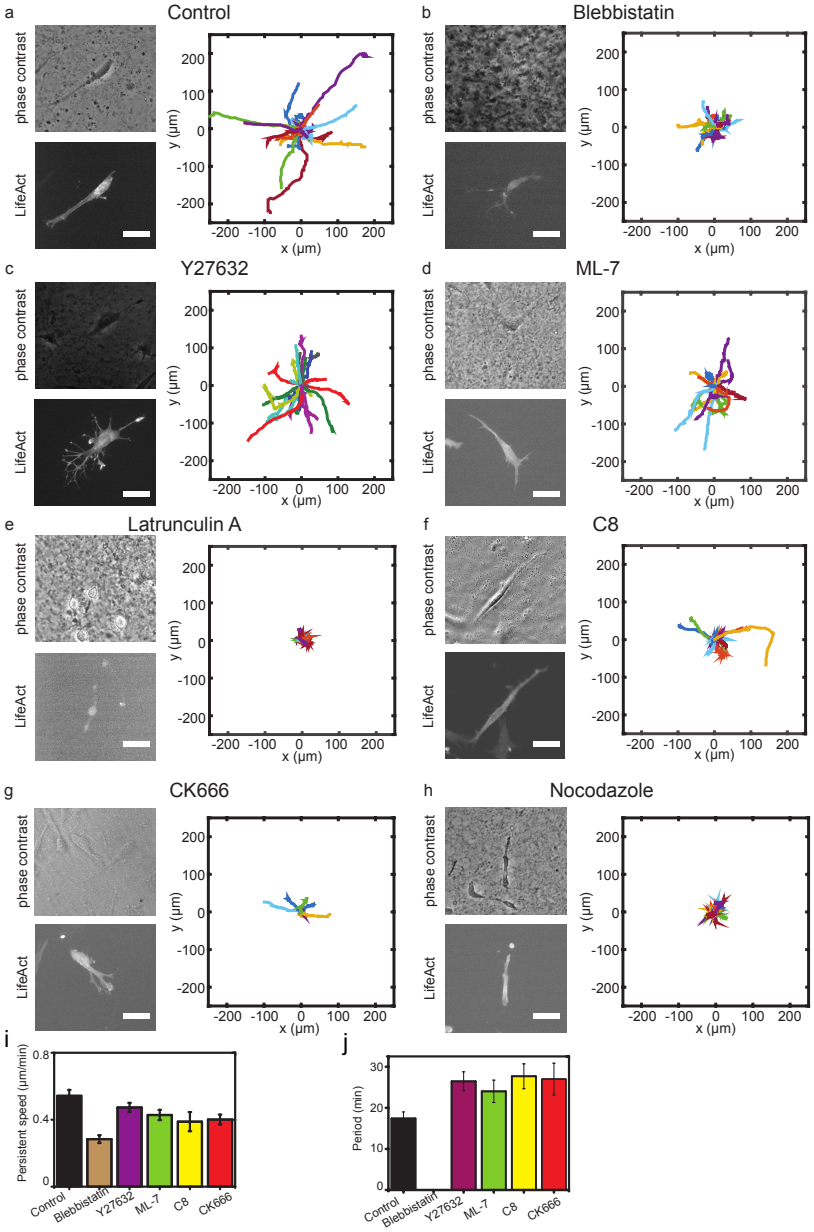

FIG. S3. Cell motion in CDM is modified in the presence of specific inhibitors. Typical trajectories of the control experiment over 5 hours, in (a), are compared to data acquired in similar conditions but where cell morphologies are altered in the presence of: (b) blebbistatin; (c) Y-27632; (d) ML-7; (e) latrunculin A and (h) nocodazole. Treatments with C8, in (f),[18] and with CK666, in (g), do not alter the cell morphology. Trajectories are shorter for all drugs except Y-27632. No migration is observed in the case of nocodazole and latrunculin A; see also Movies 10-12. Typical cell morphologies are shown for each condition, using bright field, on the top panel, and Life-Act labeling, on the bottom panel. i) Persistent speed for control and cells treated with 10μM Y-27632, 25μM blebbistatin, 10 μM ML-7, 100 μM C8 and 50 μM CK666. (Average values are reported in Material and MethodsI B 6 j) Average of the period of the cell speed calculated by autocorrelation analysis of speed projected on axis of migration. Scale bars 25μm.

B. Material and Methods

1. Preparation of CDM

For the CDM preparation (see Suppl. Fig. 1a and [19]), a glass coverslip (CS) was incubated with 1% gelatin (gelatin from cold water fish skin, Sigma) and put at 37^oC in the incubator for $1h$. After two washing steps with 1% PBS, the CS was incubated with the gelatin solution for 20 min at room temperature with 1% glutaraldehyde (Sigma). The CS was rinsed again twice with PBS before incubation for $20-30$ min with 1 M glycine (Sigma). Subsequently the CS was washed twice with PBS before plating of the NIH3T3 fibroblasts. Cells were plated at high density in order to produce CDMs. For NIH3T3, this corresponded to a cell density of 10^5cells/mm in the Petri dish. The culture medium was supplemented with 50μg/ml L-ascorbic acid and changed every two days. The culture was maintained for $8-9$ days. Cells were removed by a lysis medium consisting of 20mM NH4OH and 0.5% Triton (both Sigma) in 1x PBS after two washing steps with PBS. The pre-warmed lysis medium was carefully pipetted on the CS and incubated for up to 10 min at 37^o C in the incubator. PBS solution was added and the CDM stored at 4^oC. The day after, the PBS solution was carefully changed three times to remove residues of Triton. The matrices were covered with PBS and stored for up to one month at 4^oC. For alignment purposes after acquisition, beads (200nm, BioSpheres) were spin-coated on the CS before incubation with gelatin. Beads for optical tweezers measurements (L4530, Sigma) were inserted when seeding the cells. For visualization of fibronectin inside the CDM, two methods were used with no apparent differences : we prepared a stable cell line expressing fluorescent fibronectin (construct kindly provided by Erickson laboratory, Duke University), alternatively, fluorescently labelled FN (Cytoskeleton Inc.) was added to the culture.

2. Cell culture, transfection and drugs

Cells were cultured at 37^o C under 5% CO2 with a culture medium, high glucose D-MEM with 1% penstrep (Penicillin Streptomycin, Fisher Scientific) supplemented with 10% Bovine Calf Serum (BCS, Sigma). Transfections were performed with Lipofectamin 2000 (Invitrogen) using a standard protocol, and the following constructs were used : mCherry Lifeact, GFP-NMHC2A (kindly provided by Ewa Paluch lab, UCL), RFP zyxin (kindly provided by Anna Huttenlocher lab, University of Wisconsin-Madison) or mCherry MRLC2A (Addgene). For experiments with inhibitors, ROCK inhibitor Y-27632 was used at a concentration of 10μM, microtubule de-polymerising agent nocodazole at 10μM, myosin II inhibitor blebbistatin at 25μM, MLCK inhibitor ML-7 at 10μM, F-actin depolymerizing agent latrunculin A at 1μM, Arp2/3 inhibitor CK666 at 50μM (all Sigma) and lamellipodia growth promoter C8 at 100μM [18]. Before drug addition, we performed a control acquisition of at least one hour. To prevent flows, defocusing or potential damage of the CDM during manipulation, medium with drugs was added to the running experiment without removing the medium to reach the target concentration.

3. Time-lapse imaging and laser ablation, Optical set-ups, Electron Microscopy

We used a Nikon Ti Eclipse inverted microscope equipped with a Lambda DG-4 (Shutter Instruments Company), a charge coupled device (CCD) camera CoolSNAP HQ2 (Photometrics), a temperature control system (Life Imaging Services) and, if needed, CO2 control. The objectives were the following : PhLL 20x (air, 0.95 NA, phase contrast, Nikon), a Plan Apo 60x objective (oil, 1.40 NA, DIC, Nikon) and a x40 (air, 0.95 NA, Olympus) objectives with a home-made adapter to fit the Nikon microscope. Images were acquired with the NIS Elements software (v3.10, SP3, Nikon) and then exported for further processing. We also used a CKX41 inverted phase-contrast microscope (Olympus) with a cooled CCD camera (Hamamatsu). The system was equipped with a temperature control (Cube box system) and 4x, 10x, 20x and 40x phase contrast air objectives. For confocal imaging, we used a Leica TCS SP5-MP inverted microscope equipped with a Leica Application Suite Advanced Fluorescence LAS AF 2.6.3.8173/LAS AF 3.1.2.8785 acquisition system with hybrid detectors (HyD), photomultiplier tube (PMT) and a heating system (Cube box system); with a HCX PL APO 63X oil objective (1.4 NA, Leica). Additionally, a Leica DMI6000 inverted microscope was used as a spinning disk, equipped with a Andor iQ 1.9.1 acquisition system, Yokogawa CSU22 spinning disk unit and a heating system (Tokai Hit Stage Top Incubator, INU incubation system for microscopes). A HCX PL APO 40x oil objective (1.25 NA, Leica) was used. The time between two frames ranged from 10s to 5min and typical exposure time was $100-200$ ms. The software Imaris was used for reconstructing and animating 3D data sets.

For laser ablation, a Leica TCS SP8-MP based on a Leica DM6000 CFS upright microscope was used, equipped with a Leica Application Suite Advanced Fluorescence LAS AF 2.6.3.8173/LAS AF 3.1.2.8785 acquisition system with photomultiplier tube (PMT) and hybrid detectors (HyD) and an environmental chamber for temperature control

(Cube box system). A 25X HCX IRAPO L water objective (0.95 NA, Leica) was used and ablation performed with infrared pulsed laser (Coherent Vision II with pre-compensation). FRAP module was used with point ablation with a wavelength set at 800 nm and an exposition time of 100-200 ms. During experiments, parameters such as laser power and gain were set to minimum to have the smallest cut possible while maintaining cell and CDM integrity.

Native CDMs with integrated cells were imaged by electron microscopy (EM). To have the z-information of CDM, they were grown on Polystyrene sheets. The CDMs were fixed by immersion in 2.5% glutaraldehyde and 2.5% paraformaldehyde in cacodylate buffer (0.1 M, pH 7.4), and post-fixed in 1% osmium tetroxide in 0.1M cacodylate buffer for 1 hour at 4^o C. The samples were dehydrated through graded alcohol (50, 70, 90, 100%), and critical point dried with hexamethyldisilazane. After mounting on stubs with conductive carbon adhesive tabs, the CDMs were coated with gold-palladium in sputter coater (BAL-TEC SCD 005). For imaging along the z-axis, CDMs were cut and mounted upright with conductive carbon tape. Then they were examined by XL SIRION 200 FEG SEM (FEI company, Eindhoven, The Netherlands).

4. Image Analysis

Images were pre-treated for image analysis. In the case of a z-stack, images were projected with average or maximal projection and outliers were removed with Remove Outlier function of ImageJ. Then deformation was tracked in 2D. A "pyramidal implementation" of KLT tracker method was used to detect deformation in the mesh [19]. This method is based on Kanade-Lucas-Tomasi algorithm and follows bright features from one image to another. Therefore, a textured patch with high intensity variation in x and y is required. A multi-resolution pyramid of the image intensity and its gradients are computed before tracking is performed. Then the KLT algorithm is first applied to lower resolution image, where it detects coarse movement before a higher resolution image is taken for fine movement detection. After having reached the maximum iteration steps for all pyramid levels, the displacement of the feature is extracted (between two frames). The Computer Vision Toolbox for MatLab was used with a customary written code with number of features varying between 5000-10000 and a minimum distance from 8-14 px depending on image size, making sure that features were sufficiently spaced. Parameter window interrogation size was set to 40 px and maximal iteration to 20 px. The number of pyramids was two for all calculations. For each image an overlay of displacement vectors and phase contrast or fluorescent image of cell was generated. Drift calculation was performed with maximum of 40 px features with a minimum distance of 8 px with a window size of 20 px and one pyramid. The displacement due to drift was subtracted from the cell induced displacement of the mesh.

Once the displacement of the meshwork calculated via the KLT feature tracker, the displacement of the matrix was projected onto a line going through the cell axis in order to observe 1D matrix displacement and the heatmap of displacement plotted (Fig.2). The matrix displacement amplitude is colour coded in the heatmap. To highlight the cell position in the heatmap, cell features such as nuclear front, back and cell tail were tracked and plotted in the heatmap. To investigate recurring patterns of matrix displacement along the cell axis, autocorrelation analysis was performed on the projected matrix displacement. The displacement was averaged over a region of 2-5 um either at the cell back or the cell front both regions delimited by nucleus back over a time period where a cell was either migrating or not migrating. Average matrix displacement was subtracted to reduce background and autocorrelation performed via Matlab using the xcorr function with coefficient normalization so that the autocorrelation at zero lag equals 1.The highest peak next to 0 was extracted. Graphs where no peak could be identified were discarded. To compare matrix displacement at two distinct positions along cell axis, crosscorrelation analysis was performed with the same parameters as for the autocorrelation. In this case the highest (or deepest peak) was extracted. Graphs where no peak could be identified were discarded.

5. Elasticity CDM measurements by optical tweezers

CDM with fluorescent beads were mounted on a holder and placed on an inverted microscope (Olympus IX71). A Spectra Physics YAG laser (1064 nm) was used and focused through a high numerical oil immerse on objective (Zeiss achromat x100 1.25 NA). We acquired the movies with a second objective (Olympus X40 0.6 NA) associated with a CCD camera (DCC3240C, Thorlabs). The setup was controlled by LabView 9 (National Instruments). Beads were centered in the optical trap (Suppl. Fig. 1e). The position of the CS (bottom of CDM) was registered to obtain the z position of the measured beads in the CDM. Stage was moved in 0.2μm/s or 0.1 nm/s steps, covering a distance of $2-4\mu$m in x/-x and y/-y directions (see Movie 1). The laser power was calibrated with beads in solution. Subsequent data processing was performed with ImageJ bead Tracker Plugin and further post-processed with IgorPro Wavemetrics.

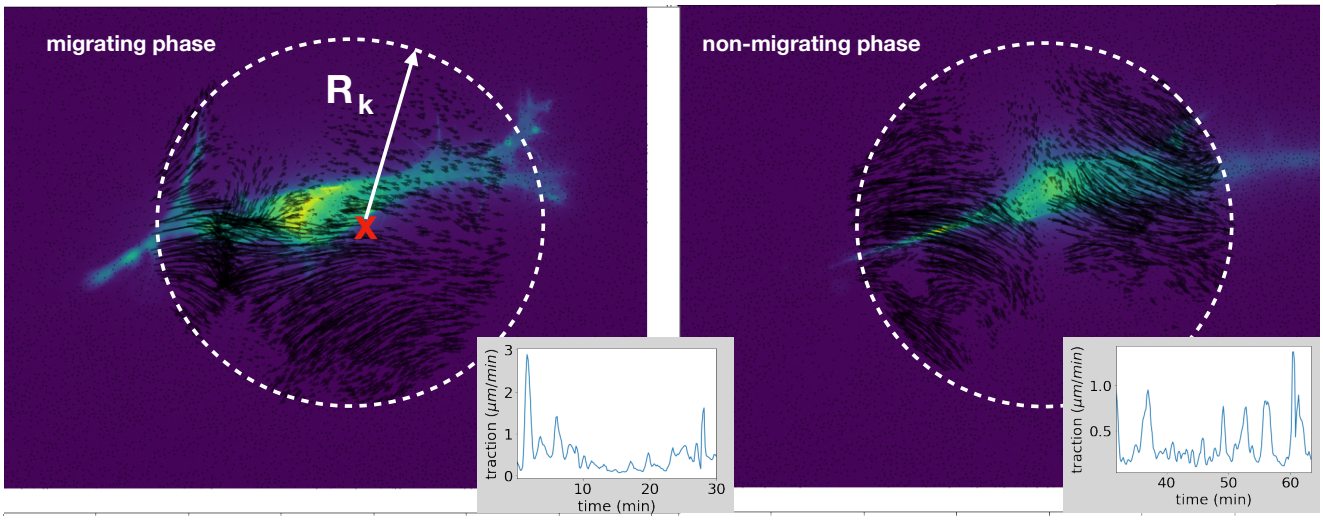

FIG. S4. Method to compute the multipolar terms illustrated by using the same cell of Fig.4(b), which in the course of the same experiment shows a transition between migrating phase, (left), and non-migrating phase, (right). (Left): experimental image showing a cell in light blue, and the vector field restricted to a circular region used to compute the multipoles. The center (red cross) is obtained starting from the cell centre position and searching for the coordinates (X^*, Y^*) that minimize the monopole term. We consider regions enclosed by different radii R_k, with $k = 1, 2, ...$ and compute the multipoles in each of these regions. We then compute the average values of the multipolar terms and obtain error bars as the standard deviations over all these regions. Insets: average traction, computed as the average of the absolute value of the rate of deformation field within the circular region. The traction in the non-migrating phase is slightly smaller than the traction during the migrating phase but the two values are comparable. (Right): the cell does not move because the topology of the vector field has changed compared to the migrating phase, showing now mainly a dipolar field.

6. *Average values of period, deformation and persistent speed*

We quantified the fibronectin network dynamics, Fig.2c, and we measured periods of 10.2 ± 1.4 mins for the front and 9.9 ± 1.1 mins for the back of the cells and amplitudes of typically 2.5 μm were reached. Non-motile cells also exhibit local spots of contraction-extension, Fig.3a, with periods of matrix displacement of 8.1 ± 1.3 min for the front and 7.1 ± 1.2 min for the back dipole. For nococazole, cells switched polarity in the course of the experiments and only a single period of 9.5 ± 1.2 min was extracted. In Figure 3c, Persistent speed are: $0.54 \pm 0.04\mu$m/min (control); $0.47 \pm 0.02\mu$m/min (cells treated with Y-27632), $0.28 \pm 0.02\mu$m/min (blebbistatin); $0.43 \pm 0.03\mu$m/min (ML-7); $0.39 \pm 0.06\mu$m/min (C8) and $0.40 \pm 0.03\mu$m/min (CK666). Average oscillation periods are: 15.00 ± 1.25 min (Control); 20.7 ± 1.3 min (Y-27632); 24 ± 3 min (ML-7); 27 ± 3 min (C8); and 27 ± 4 min (CK666).

7. *Multipolar expansion*

To quantify the cell-matrix interaction, deformation, we determine the substrate velocity vector field $u_i^{(n)}$ as described in the main text. The component i at position n of the mesh of the substrate velocity $u_i^{(n)}$ has the same topology of the traction force vector field [15] (which we do not compute here). We then calculate the monopole vector $M_i = \sum_n u_j^{(n)}$, the dipole matrix $S_{ij} = \frac{D_{ij}+D_{ji}}{2}$ and the quadrupole matric $Q_{ijk} = \sum_n \Delta_i^{(n)} \Delta_j^{(n)} u_k^{(n)}$, where $D_{ij} = \sum_n \Delta_i^{(n)} u_j^{(n)}$, where $\Delta_i^{(n)}$ is the i-th component of the vector joining the cell centre (defined below) and the point n on the mesh. We also compute to total traction defined as $\sum_n |u^{(n)}|$. We then consider the projection of these quantities on the main axis identified by the average direction of the cell trajectory and we call these components the main monopole, M, the main dipole, D, and the main quadrupole, Q. For cells which are non-migrating (i.e. that do not move at all) but are still elongated we identify the main axis as the cell axis.

A cell that migrates spontaneously (i.e. in absence of external forces) can be viewed as a force-free body, hence in the absence of inertia the sum of all the traction forces add up to zero [15]. Thus the monopole should be zero. In our experiments, 3D imaging is challenged by a limited and asymmetric field of view which lead to a nonzero value of the monopole. To reduce these imaging asymmetries, the traction, monopole, dipole and quadrupole are computed and

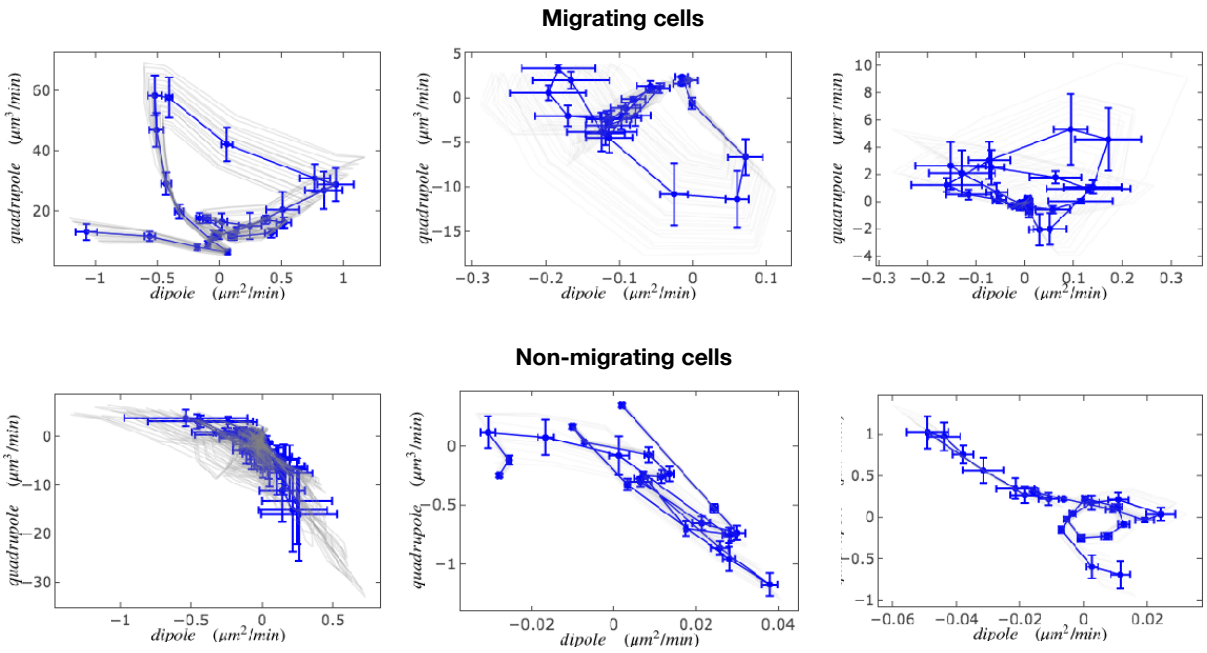

FIG. S5. Comparison between cycle curves obtained in different experiments for different migrating (left panels) and non-migrating (right panels) cells. We observe a variability in the traction forces for both migrating and non-migrating cells, but we exclude that non-migration is due to lack of traction (compare top left and right panels). For non-migrating cells exerting a single force dipole, the quadrupole is expected to be zero. The non-zero quadrupole, seen to be correlated with the dipole for non-moving cells, may be due to asymmetries in the field of view, see above (Section I B 7).

averaged over discs (Fig.S4) of increasing radius R_k, $k = 0, 1, ...M$ starting from a minimum radius $R_0 \sim 20\mu m$ and up to a maximum radius R_M defined as the biggest radius such that the circular region is fully contained within the boundaries of the experimental images. To minimise the spurious monopole, the center of the disc is varied around the apparent cell center (obtained from cell tracking) and the location for which the monopole is minimum is adopted as the center of the discs on which the dipoles and quadrupoles are computed. This is done at every time step.

Additional examples of cycles for migrating and non-migrating cells are shown in Fig.S5. As in the main text, the cycles shown for migrating cells are obtained by first identifying intervals of time with clear oscillating behavior in the speed and focusing on that time interval when we compute the multipolar expansion. For cells which are non-migrating, we cannot apply this scheme as we have no notion of oscillating speed, thus the choice in Fig.S5 is somehow arbitrary. Nonetheless, we find that the areas of cycles for non-migrating cells are systematically negligible when compared to the areas of migrating cells.

C. List of Movies

- Movie 1 : CDM is elastic, as shown by optical tweezer characterization, time in mm:ss.
- Movie 2 : Cell deforms the CDM, time in hh:mm.
- Movie 3 : Cells deform the fibronectin network in yellow while moving, scale bar 20 μm, time in hh:mm.
- Movie 4 : Cells motion in 3D with CDM and the associated focal contacts dynamics (fibronectin in yellow and zyxin in red), time in hh:mm:ss.
- Movie 5 : Microtubule asymmetric distribution (left) is associated to cell polarity during motion, time in hh:mm.
- Movie 6 : The volume of the nucleus impedes cell motion, scale bar 25 μm, time in hh:mm.
- Movie 7 : Phase-shift between local dipoles is associated to cell motion; cell motion (left, LifeAct red), fibronectin network deformation (center yellow), merge, time in hh:mm:ss.
- Movie 8 : Local laser ablation triggers the local recruitment of actin and local contraction, time in mm:ss.

- Movie 9 : Induced dipoles (indicated by arrows) trigger cell motion, time in mm:ss.
- Movie 10 : Cell motility in the presence of blebbistatin added at time 0, time in hh:mm, scale bar 25 μm.
- Movie 11 : Cell motility in the presence of latrunculin A added at time 0, time in hh:mm, scale bar 25 μm.
- Movie 12 : Cell motility in the presence of nocodazole added at time 0, time in hh:mm, scale bar 25 μm.